buildings

MDPI

Article

Influence of Boundary Conditions on the Estimation of Thermal Properties in Insulated Building Walls

Manon Rendu [1,2,3], Jérôme Le Dréau [1,2,*], Patrick Salagnac [1,2] and Maxime Doya [1,3]

[1] LaSIE (UMR CNRS 7356)—La Rochelle University, Avenue Albert Einstein, 17000 La Rochelle, France; manon.rendu@plateforme-tipee.com (M.R.); patrick.salagnac@univ-lr.fr (P.S.); maxime.doya@univ-lr.fr (M.D.)
[2] 4evLab, La Rochelle University, CNRS, EDF, Avenue Albert Einstein, 17000 La Rochelle, France
[3] TIPEE (Technological Platform), Rue Isabelle Autissier, 17140 Lagord, France
* Correspondence: jledreau@univ-lr.fr

Abstract: The objective of this study is to evaluate the ability of inverse techniques to estimate the resistance and the capacity of a highly insulated multilayer wall under real weather conditions. The wall is equipped with temperature sensors inside and on its inner and outer surfaces, and the boundary conditions have been measured over a 14-day period. Uncertainties on various parameters of the model are evaluated, including internal and external convective heat transfer coefficients (±20% and ±7 $W.m^{-2}.K^{-1}$ respectively), external long-wave heat transfer coefficient (±0.15 $W.m^{-2}.K^{-1}$) and solar absorption coefficient (±0.06). A sensitivity analysis demonstrated the high correlation with some parameters defining the thermal performance of the walls (thermal resistance or capacity). A solution is proposed to limit the number of identified parameters, while allowing the identification of the thermal resistance and the thermal capacity of the walls. There are two cases: either the weather conditions are accurately measured (temperature, short- and long-wave radiation) and the thermal characteristics can be assessed, or intrusive sensors are installed, and the thermal characteristics can be evaluated more accurately.

Keywords: heat transfer; building envelope; walls thermal transmittance; modelling; inverse methods; boundary conditions; in-situ measurements

Citation: Rendu, M.; Le Dréau, J.; Salagnac, P.; Doya, M. Influence of Boundary Conditions on the Estimation of Thermal Properties in Insulated Building Walls. *Buildings* **2024**, *14*, 3706. https://doi.org/10.3390/buildings14123706

Academic Editor: Alessandro Cannavale

Received: 18 October 2024
Revised: 14 November 2024
Accepted: 15 November 2024
Published: 21 November 2024

1. Introduction

Many factors influence the energy consumption of buildings, but the building envelope plays a key role in the overall performance. Envelope heat losses are affected by conduction through opaque walls, by conduction and radiation through windows, by air leakage [1] and also by deterioration in performance over time [2].

Heat transfer by conduction can be characterized by the physical properties of each wall material. From these physical properties and from geometrical data, it is possible to determine the *R*-value and *C*-value of the wall components, which correspond to the thermal resistance and the thermal capacity, respectively [3]. Standard laboratory tests have been developed to evaluate material properties as described in [4,5]. However, these methods cannot be applied to the wall of a constructed building without causing damage.

Alternative methods have been developed to measure the thermal characteristics of the building envelope, either already built or under construction [6], such as the heat flux meter method [7], which consists of calculating the thermal transmittance of walls using two-temperature measurements (inside and outside) and a heat flux meter. However, such a method takes several days, the external surface should not be exposed to solar radiation, and the thermal capacity cannot be estimated. In addition, common uncertainties associated with the heat flow measurement make the identification of high thermal resistances difficult [8]. Teni [9] shows that the methods based on a simple model (where the resistance is expressed by an analytical equation) lead to high uncertainties, except when the boundary conditions are controlled, as in the case of a hot box.

A wide range of other methods are available, mainly using inverse techniques [10–12]. They consist of minimizing the gap between a model and the measurements obtained from an experiment in order to infer the unknown parameters of the model. With respect to the opaque walls discussed in this article, inverse techniques can use a wide variety of models such as quadrupole models [13,14], response factor models [15,16], resistance–capacitance models [17,18] or ARX models [7,19–21]. Furthermore, inverse techniques can be deterministic approaches [22], Bayesian analyses [23–25] or genetic algorithms, for instance [26,27]. These methods can use either temperature measurements (single point measurements with thermocouples or PT100 or mapped measurements with an infrared thermal camera [28]), heat flux measurements or both. The main drawback of these methods is that most of them do not allow the identification of the thermal capacity of the wall. If the method estimates the *C*-value, heat flux meters are usually required [16,23,25]. Indeed, the method described in this article is designed to be used on highly insulated multilayer walls ($R > 4$ m^2.K.W^{-1}), and heat flux meters do not seem to be suitable for measuring low heat fluxes with sufficient accuracy (<5 W.m^{-2}), since in such cases, the signal-to-noise ratio is low. The aim of the method is to avoid the drawback of heat flux meters and addresses an alternative way using appropriate temperature measurements. Moreover, this method is intended to be used in real weather conditions, which requires particular attention to be paid to the measurement of boundary conditions. In contrast to a laboratory, where these conditions are controlled, the heat exchange with the wall is strongly influenced by the wind or the sun, for example.

In the literature, several authors have investigated the influence of boundary conditions on the identification of the thermal characteristics of a building element. Many studies recognize the significant influence of convective heat transfer coefficients on the U-value of walls for infrared thermographic methods (e.g., [29]). For contact-based methods, De Rubeis et al. [30] observed a large deviation of the convective heat transfer coefficient in a guarded hot-box environment compared to default values (−35%). In situ, Evangelisti et al. [31] observed differences in the *U*-values from 0.5 to 0.9 W.m^{-2}.K^{-1}, depending on the heat transfer coefficient correlations. François et al. [32] also showed the large variations of the internal heat transfer coefficient (between 6 and 12 W.m^{-2}.K^{-1}) under transient conditions. To reduce the influence of uncontrolled boundary conditions on the identification process, a sandwich structure evaluation method was developed by Derbal et al. [33]. An uncertainty below 7% was achieved, but the construction element was limited to single layer materials of PVC, EPS, plaster or concrete. From these different studies, it can be seen that the influence of convective heat transfer is recognized. However, the influence of radiant properties is rarely evaluated for contact-based methods, and these studies are also limited to walls with relatively low thermal resistance ($R < 4$ m^2.K.W^{-1}).

The aim of this paper is therefore to evaluate the performance of inverse techniques for highly insulated multilayer walls under a range of boundary conditions. The calculation of uncertainties on the estimated thermal characteristics is also a key point.

A lightweight, highly insulated wall has been installed in an experimental facility and tests have been carried out. The wall is equipped with temperature sensors on its surfaces and inside. The identification technique (deterministic approach) is applied to a resistance–capacitance model based on temperature measurements, in order to identify the thermal characteristics of walls under real weather conditions.

Estimation of the thermal conductivity and capacity (λ and $\rho.c$) of the wall materials allows calculation of the *R*- and *C*-values, which describe the thermal characteristics of an opaque wall. An inverse technique has been applied to both synthetic (model-based) and measured experimental datasets. The use of synthetic values allows the calculation of uncertainties associated with the boundary conditions.

The first part of this paper presents the case study and the experimental setup. The reference and the resistance–capacitance models are then described and numerically validated. The inverse technique is then introduced. Finally, the effects of two external boundary conditions are discussed in the results section.

2. Experimental Facility and Boundary Conditions

2.1. Case Study

The lightweight wall that was tested was a wall consisting of three homogeneous layers. The first and the third layers were made of moisture-resistant plywood (*pl*), and the second layer was made of polyurethane (*PUR*). Five sensors were installed at the locations S_{out}, $S_{1\text{-}2}$, S_2, $S_{2\text{-}3}$ and S_{in}, as shown in Figure 1.

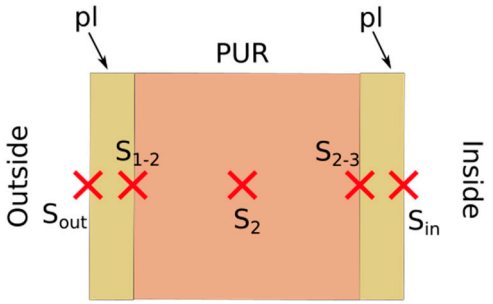

Figure 1. Locations of sensors in the wall.

The layers of the lightweight wall and their material's properties are described in Table 1, where e is the thickness. Uncertainties are those reported by the manufacturers or found in the literature. If they are missing, ±10% is used as a default value [34].

It is possible to calculate the theoretical R- and C-values of this wall using Equation (1).

$$\begin{aligned} R &= \sum_i \frac{e_i}{\lambda_i} \\ C &= \sum_i e_i \, \rho_i \, c_i \end{aligned} \tag{1}$$

The following theoretical values have been calculated: $R = 5.4 \pm 0.5$ m^2.K.W^{-1} and $C = 53 \pm 8$ kJ.m^{-2}.K^{-1}.

The shortwave absorptivity α_{SW} is a property derived from a measurement performed on a spectrophotometer with an integrating sphere. The value depends on the reference solar spectrum standard used and the sample analysed. The value found was 0.26 ± 0.06.

The longwave absorptivity α_{LW} is equal to the hemispherical emissivity of the surface $\varepsilon_{LW,}$ taking into account uniform grey and diffuse surfaces. In [35], it is stated that ε_{LW} = 0.9 is «usually appropriate for internal and external surfaces» in buildings. An uncertainty of ±0.02 has been defined according to [36].

Table 1. Material properties of the wall.

Layers		**Properties**			
Material	Code	λ	ρ	c	e
Plywood	*Pl*	0.21 ***	710 ± 10 *	1400–1800 ***	0.021 **
Polyurethane	*PUR*	0.023 *	32.5 ± 2.5 *	1400 ***	0.12 **

Sources: * manufacturers and/or official documents. ** measurement or numerical study output. *** technical document ([37,38]).

2.2. Experimental Setup

To test construction elements, outdoor test cells can be used to account for real climatic environments [39]. In this study, it consisted of a highly insulated cell surrounded by a thermal guard that was kept at a constant temperature. One of its faces was exposed to real weather conditions; it was the façade that was tested. A large amount of sensors were set up on this equipment (full weather station, temperature probes in the walls). A heating system was used to simulate different temperature scenarios, allowing the indoor and outdoor conditions to be decoupled during identification.

The experimental data sets come from the facility where the lightweight wall was installed. This facility is shown in Figure 2.

(**a**) (**b**) (**c**) (**d**) (**e**)

Figure 2. Photos of the experimental setup: (**a**) outdoor air temperature sensor; (**b**) radiometers; (**c**) sonic anemometer; (**d**) outdoor surface temperature sensors; (**e**) indoor air temperature sensors with ventilated shield and indoor surface temperature sensors.

With respect to indoor conditions, the indoor air temperature ($T_{air,in}$) was measured by six four-wire resistance thermometers (Pt100 resistance probes) protected by ventilated radiation shields located at a distance of 0.6 m from the wall at three heights (0.8, 1.6, 2.2 m) in order to check the homogeneity of the air temperature. The surface temperature of the wall (9 sensors inside S_{in} and 9 sensors outside S_{out}) and the surface temperature of each surface of the test cell (whose average gives $T_{LW,in}$) were measured by four-wire resistance thermometers located in the center of each wall.

The wall was monitored by four-wire resistance thermometers installed at three different depths ($S_{1\text{-}2}$, S_2, $S_{2\text{-}3}$) as shown in Figure 1.

With respect to outdoor conditions, the radiation was measured by two devices installed vertically near the wall: a pyrgeometer that measured impinging longwave radiation integrated within wavelengths ranging between 4 and 40 µm and a pyranometer which measured global shortwave irradiance integrated within wavelengths ranging between 0.3 and 4 µm. The output of the pyranometer is the solar radiation Q_{SW}. The outputs of the pyrgeometer are the temperature of the sensor T_{pyrgeo} and the net radiation Q_{net}, i.e., the radiation received by the device, called $Q_{\rightarrow|}$, minus the radiation emitted by the device (considered as a black body). Using these two values, it is possible to calculate the brightness temperature T_b, which is "the temperature of a black body that would emit the same amount of radiation as the targeted body in a specified spectral band" [40] as presented in Equation (2).

$$\begin{aligned} Q_{net}(t) &= Q_{\rightarrow|}(t) - \sigma\, T^4_{pyrgeo}(t) = \sigma T^4_b(t) - \sigma\, T^4_{pyrgeo}(t) \\ \rightarrow T_b(t) &= \left[\frac{Q_{net}(t)}{\sigma} + T^4_{pyrgeo}(t)\right]^{1/4} \end{aligned} \quad (2)$$

The outside air temperature $T_{air,out}$ was measured using a four-wire resistance thermometer protected by a radiation shield.

The wind speed and direction were measured by the sonic anemometer shown in Figure 2c, which was installed 4 m above the roof of the building (i.e., 15 m above the ground). The wind speed close to the façade v_{wind} (i.e., 2.5 m above the ground) was estimated from the wind speed measured by the anemometer using the conversion method presented in [41] and considering a flat terrain with some isolated obstacles.

Details of the equipment used to measure each physical variable are given in Table 2.

Table 2. Details on devices used for measurements.

Physical Variable	Sensor	Acquisition	Accuracy
Indoor air temperature	PT100 1/5 B DIN, 4 wires (TCSA)	KEYSIGHT 34980A	±0.15 °C *
Surface temperature	PT100 1/3 B DIN, 4 wires (TCSA)		
Interface temperature			
Outdoor air temperature	PT100 (VAISALA HMP1550)	COMPACT DAQ NI 9188	
Shortwave radiation	SMP21 (KIPP AND ZONEN)	RS 485—Modbus	±3 W.m^{-2} **
Brightness temperature	SGR4 (KIPP AND ZONEN)		±0.7 °C **
Wind velocity	WINCAP Ultrasonic WMT701 (VAISALA)		±0.1 m.s^{-1} **
Wind direction			±2° **

* Estimated from calibration and technical documents. ** From technical documents.

2.3. Experimental Boundary Conditions Measurement

The dataset came from a test called the *ROLBS case*, which stands for "Randomly Ordered Logarithmic Binary Sequence" [42]. It generated heating sequences of variable time duration in order to decorrelate the indoor and outdoor boundary conditions. The *ROLBS case* lasted for 14 days during the winter season with a measurement time step of 30 s. A moving average was used to obtain a time step of two minutes and thus reduce the amount of data. The measured data are shown in Figure 3. The whole dataset was divided into 3 parts: initialization, identification and validation.

Two typical weather days were selected from the *ROLBS case*, called the *typical sunny day* and the *typical cloudy day*. As shown in Figure 4, during *the typical cloudy day*, indoor temperature was almost constant. The outdoor temperature was about 10 °C, and the solar radiation varied due to clouds. The westerly wind speed was high (about 13–14 m.s^{-1}). During the *typical sunny day*, the indoor temperature was also almost constant. The outdoor temperature was between 7 and 20 °C. The solar radiation curve shows a cloudless day. The wind speed from south-east was low (about 2–3 m.s^{-1}). Both cases lasted 24 h.

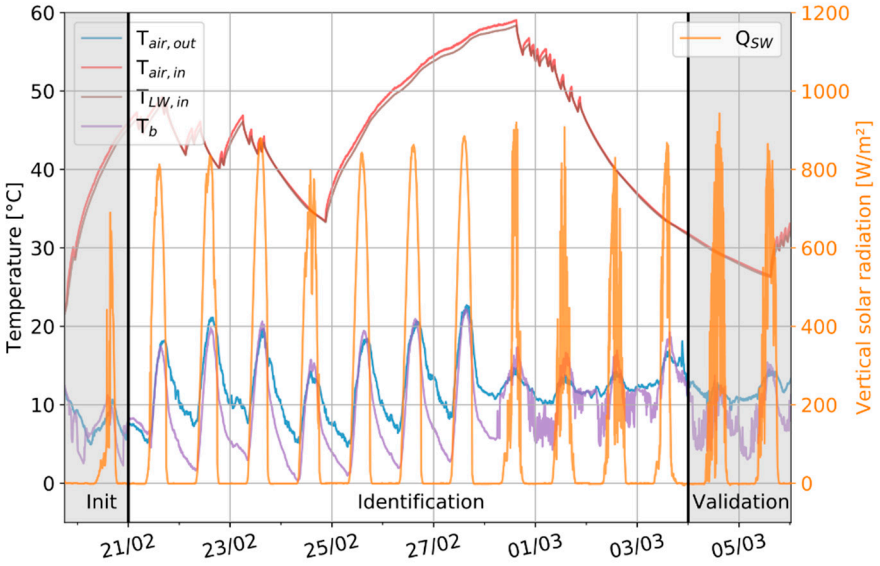

(**a**)

Figure 3. *Cont.*

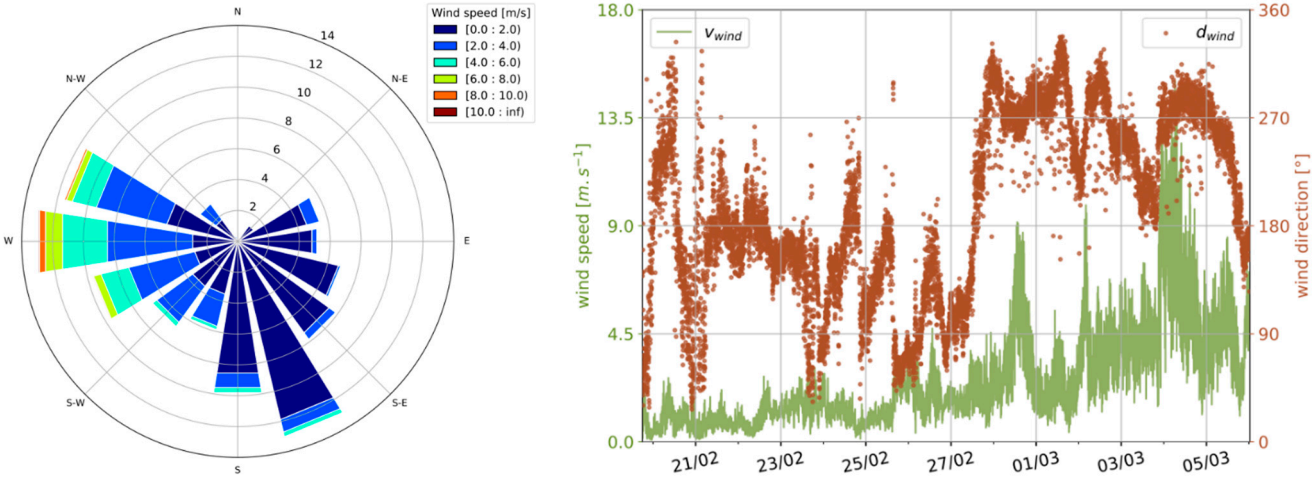

(**b**) (**c**)

Figure 3. Boundary conditions for the *ROLBS case:* temperature and solar radiation (**a**), the related wind rose (**b**) and wind speed and direction against time (**c**).

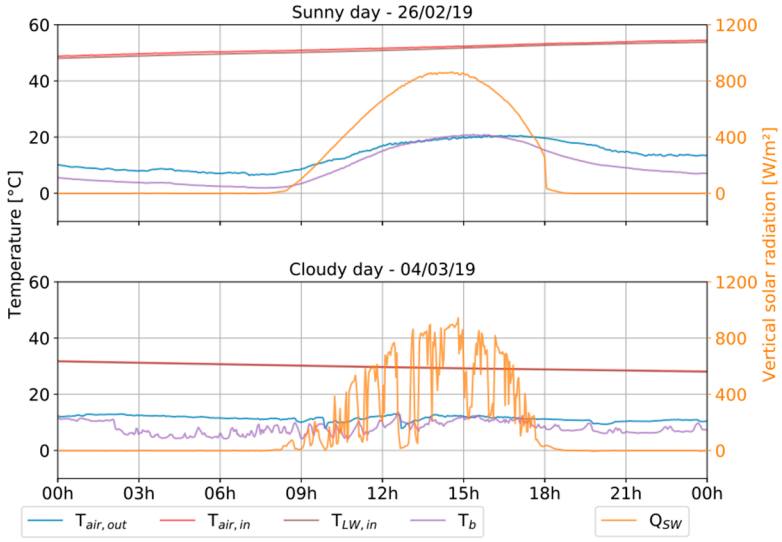

Figure 4. Boundary conditions for the *typical cloudy day* and the *typical sunny day*.

2.4. Exact Location of Sensors Inside the Wall

The position of sensors located on surfaces (S_{out} and S_{in}) or between layers ($S_{1\text{-}2}$ and $S_{2\text{-}3}$) was known. However, the position of the sensor within the insulating layer (S_2) was less certain. Sensor S_2 (shown in Figure 1) should have been in the middle of the insulating layer but could have been pushed to one side during assembly. In order to verify this hypothesis, experimental data with steady outdoor and indoor conditions were analysed. Measurements from a 24 h experimental test between 27 and 28 November 2018 were used. The difference between the indoor air temperature and the outdoor air temperature was more than 40 °C. In addition, the standard deviations of the air temperature, surface temperature and internal wall temperature measurements were less than 0.8 °C throughout the period. The temperature profile was theoretically linear. The result is shown in Figure 5. The true position of sensor S_2 was not exactly in the center of the insulation layer but was displaced inwards by 4.3 mm.

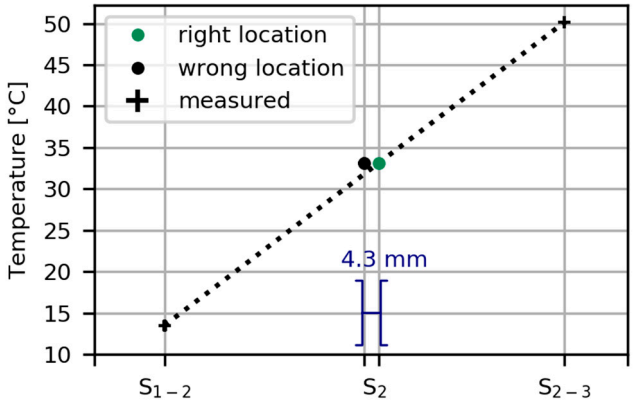

Figure 5. Estimation of location of sensor S_2 based on the temperature distribution under steady-state conditions.

3. Modelling

Only one-dimensional heat conduction in the wall was considered. Heat transfer through multilayer walls was modelled using the heat equation (Equation (3)).

$$\rho c \frac{\partial T}{\partial t} - \frac{\partial}{\partial x}\left(\lambda \frac{\partial T}{\partial x}\right) = 0 \tag{3}$$

The studied wall consisted of three layers of different materials, namely, layer 1, layer 2 and layer 3 from outside to inside as shown in Figure 6. The outer surface was at $x = 0$ and the inner surface was at $x = L$. This wall has a cross-section of 1 m^2. Figure 6 shows the five locations (S_{out}, $S_{1\text{-}2}$, S_2, $S_{2\text{-}3}$ and S_{in}) where sensors were installed. The initial conditions were the temperature values obtained assuming steady state conditions.

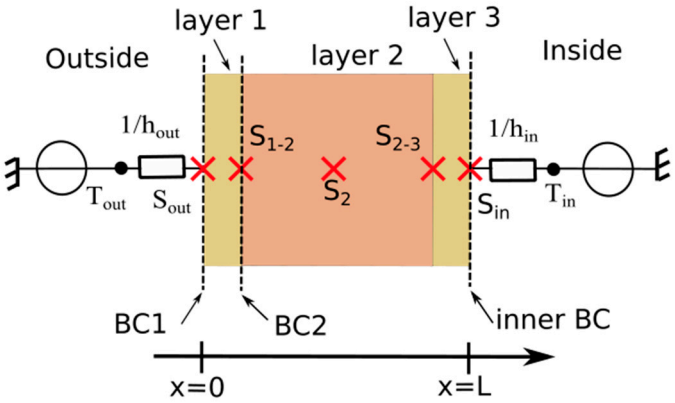

Figure 6. Location of boundary conditions and sensors.

3.1. Boundary Conditions

The influence of external weather conditions is taken into account by two types of boundary conditions (*BC*): either a Neumann condition (heat fluxes reaching the façade, see Equation (4)) is applied at the location of the sensor S_{out} (called *BC1*), or a Dirichlet condition is applied at the location of the sensor $S_{1\text{-}2}$ (called *BC2*) (see Figure 6). Dirichlet condition was not considered for *BC1*, as the objective is to use S_{out} to identify the thermal properties and avoid the use of intrusive sensors. Conversely, a Neumann condition was not considered for *BC2* as temperature sensors are more robust and accurate than heat flux sensors. In the following sections, only the models built with *BC1* are described in detail. A similar procedure was carried out for *BC2*.

The boundary conditions were conditions of the third kind, also known as Robin's conditions [43]. They can be written as:

$$\begin{aligned} Outside: \quad & \lambda_{layer1} \left.\frac{\partial T}{\partial x}\right|_{x=0} = Q_{conv,out}(t) + \alpha_{LW} Q_{LW,out}(t) + \alpha_{SW} Q_{SW}(t) \\ Inside: \quad & \lambda_{layer3} \left.\frac{\partial T}{\partial x}\right|_{x=L} = Q_{conv,in}(t) + Q_{LW,in}(t) \end{aligned} \tag{4}$$

where α_{SW} and α_{LW} are the surface absorptivity for shortwave radiations and for longwave radiations.

The indoor longwave radiative heat flux is linearized. The indoor convective and longwave radiative heat flux $Q_{conv,in}$+ $Q_{LW,in}$ is calculated in Equation (5):

$$Q_{conv,in}(t) + Q_{LW,in}(t) = h_{in}(T_{in}(t) - T_{s,in}(t)) \tag{5}$$

where $h_{in}(t) = h_{conv,in}(\mathrm{t}) + h_{LW,in}(t)$ and $h_{LW,in}(t) \approx 4\sigma\varepsilon_{LW}\left[\frac{T_{s,in}(t)+T_{LW,in}(t)}{2}\right]^3$ and $T_{in}(t) = \frac{h_{conv,in}(t)\ T_{air,in}(t)+h_{LW,in}(t)\ T_{LW,in}(t)}{h_{in}(t)}$.

Where $h_{conv,in}$ is the indoor convective heat transfer coefficient, $h_{LW,in}$ is the indoor radiative heat transfer coefficient, h_{in} is the indoor convective and radiative heat transfer coefficient, T_{in} is the indoor operative temperature and $T_{LW,in}$ is the mean radiant temperature.

The heat transfer coefficient $h_{LW,in}$ depends on the surface area of the wall, the surface area of the other walls of the test cell, their view factors and their infrared emissivity. The calculation is described in detail in [44]. In this case, the view factor is equal to 1 and the wall surface is about 10 times smaller than the combined surface of the other walls of the test cell. Thus, the approximation given in Equation (5) can be assumed to hold. The difference between the exact formula and the approximation is 1%.

The outdoor heat flux over time is the sum of the outdoor convective heat flux $Q_{conv,out}$, the absorbed longwave radiative heat flux $\alpha_{LW}\ Q_{LW,out}$ and the absorbed shortwave radiative heat flux $\alpha_{SW}Q_{SW}$. The outdoor longwave radiative heat flux is linearized. The outdoor heat flux is calculated by Equation (6):

$$Q_{conv,out}(t) + \alpha_{LW} Q_{LW,out}(t) + \alpha_{SW} Q_{SW}(t) = h_{out}(T_{out}(t) - T_{s,out}(t)) \tag{6}$$

where

$$Q_{conv,out}(t) = h_{conv,out}(t)(T_{air,out}(t) - T_{s,out}(t))$$

and

$$\alpha_{LW} Q_{LW,out}(t) = h_{LW,out}(t)(T_b(t) - T_{s,out}(t))$$

With $h_{conv,out}$ standing for the outdoor convective heat transfer coefficient, $h_{LW,out}$, the outdoor radiative heat transfer coefficient, h_{out}, the outdoor convective and radiative heat transfer coefficient, T_{out}, the equivalent outdoor temperature (of the viewed environment) and $T_{s,out}$, the outer surface temperature of the wall.

The equivalent outdoor temperature can be expressed by Equation (7)

$$T_{out}(t) = \frac{h_{conv,\mathrm{out}}(t) T_{air,\mathrm{out}}(t) + h_{LW,\mathrm{out}}(t) T_b(t) + \alpha_{SW} Q_{SW}(t)}{h_{out}(t)} \tag{7}$$

where

$$h_{out}(t) = h_{conv,\mathrm{out}}(\mathrm{t}) + h_{LW,\mathrm{out}}(t) \text{ and } h_{LW,\mathrm{out}} = 4\sigma\varepsilon_{LW}\left[\frac{T_b(t) + T_{s,out}(t)}{2}\right]^3$$

3.2. Heat Transfer Coefficients

The models described above are based on the following heat transfer coefficients: $h_{LW,in}$, $h_{LW,out}$, $h_{conv,in}$, $h_{conv,out}$. $h_{LW,in}$ and $h_{LW,out}$, which are calculated from Equations (5)

and (7). They depend on the surface temperatures ($T_{s,in}$ or $T_{s,out}$), the temperature of their surroundings ($T_{LW,in}$ or T_b) and the hemispherical infrared emissivity of the surface ε_{LW}. The uncertainty is estimated to be about ± 0.15 W.m^{-2}.K^{-1} using the propagation of uncertainties.

For convection, $h_{conv,in}$ is assumed to be equal to 2.5 W.m^{-2}.K^{-1} as defined in [35] for a horizontal heat flux. The same value is given by the correlation of Khalifa and Marshall ([45,46]) considering a room heated by a circulating fan (wall opposite to the fan). As mentioned in [46,47], the uncertainty is about $\pm 20\%$.

Convective heat transfer on external surfaces is influenced by many variables, such as local wind speed, flow regime and surface roughness. Many empirical correlations exist to estimate $h_{conv,out}$ as a function of wind speed v_{wind} and wind direction d_{wind} [48]. In this article, a simple correlation is chosen according to ISO 6946 [35], as shown in Equation (8). In our case study, it leads to a variation of $h_{conv,out}$ between 5 and 45 W.m^{-2}.K^{-1}.

$$h_{conv,out}(t) = 4 + 4\, v_{wind}(t) \tag{8}$$

In order to estimate the uncertainty of this coefficient, two other correlations were calculated: that of the ASHRAE task group which proposes a non-linear relationship to the local wind speed [49,50] and that of Liu and Harris, which makes a distinction according to the wind incidence (windward-leeward) [51]. These two models were selected, as they are quite widely used and also cover the full range of correlations found in the literature [5]. As shown in Figure 7, the correlation of Liu and Harris gives lower heat transfer coefficients, and the ASHRAE correlation is in line with the simple correlation or slightly higher. A variation of ± 7 W.m^{-2}.K^{-1} is thus considered for this parameter.

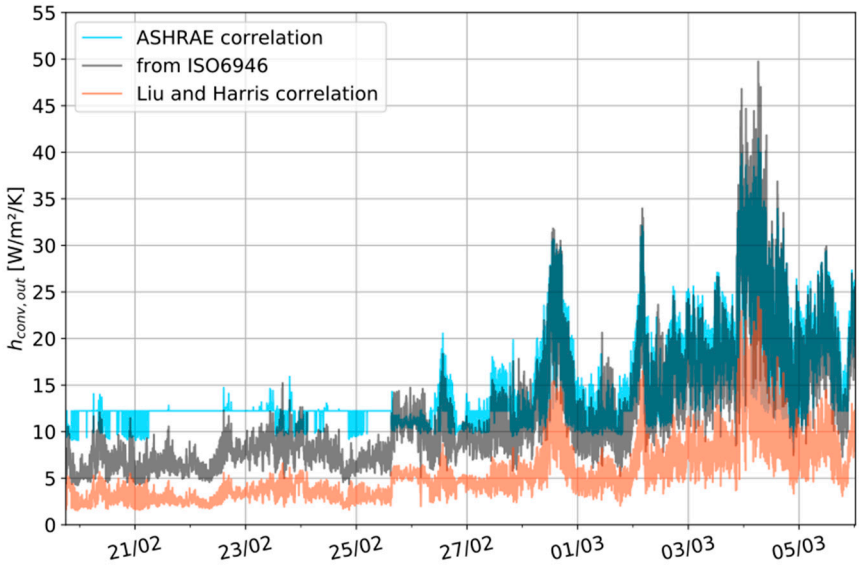

Figure 7. Outdoor convective heat transfer coefficients for different correlations in the *ROLBS case*.

3.3. The Reference Model

The *reference model* to which the *RC model* was compared uses COMSOL® 5.5 software [52]. This software is based on the finite element method. The wall is divided into 28 domains. Quadratic interpolation is used for the temperature field. The time step is set at 10 s. The boundary conditions are modelled as described above (Equations (5) and (6)), except for the absorbed longwave radiative heat flux, which is not linearized.

3.4. The Resistance–Capacitance Model

In the resistance–capacitance (RC) model, the walls are considered to be a combination of resistances and capacitances. The nodes between two layers or at the surface (indoor

or outdoor) have no capacity [53]. Resistances and capacitances are evenly distributed in each layer.

Considering a simple *RC model* with one capacity in each layer (Figure 8), also known as the *6R3C model*, the following equations are obtained:

$$diag(0, C_1, 0,\ C_2,\ 0,\ C_3,\ 0) \times \begin{pmatrix} \dot{T}_{s,out} \\ \dot{T}_1 \\ \dot{T}_{1-2} \\ \dot{T}_2 \\ \dot{T}_{2-3} \\ \dot{T}_3 \\ \dot{T}_{s,in} \end{pmatrix} = \begin{pmatrix} h_{out} & 0 \\ 0 & \vdots \\ \vdots & \\ & \vdots \\ \vdots & 0 \\ 0 & h_{in} \end{pmatrix} \times \begin{pmatrix} T_{out} \\ T_{in} \end{pmatrix}$$

$$+ \begin{pmatrix} -h_{out} - \frac{2}{R_1} & \frac{2}{R_1} & 0 & \cdots & & \cdots & 0 \\ \frac{2}{R_1} & \frac{-4}{R_1} & \frac{2}{R_1} & \ddots & & & \vdots \\ 0 & \frac{2}{R_1} & -\frac{2}{R_1} - \frac{2}{R_2} & \frac{2}{R_2} & & & \\ \vdots & \ddots & \frac{2}{R_2} & \frac{-4}{R_2} & \frac{2}{R_2} & \ddots & \vdots \\ & & \ddots & \frac{2}{R_2} & -\frac{2}{R_2} - \frac{2}{R_3} & \frac{2}{R_3} & 0 \\ \vdots & & & \ddots & \frac{2}{R_3} & \frac{-4}{R_3} & \frac{2}{R_3} \\ 0 & \cdots & & \cdots & 0 & \frac{2}{R_3} & -h_{in} - \frac{2}{R_3} \end{pmatrix} \times \begin{pmatrix} T_{s,out} \\ T_1 \\ T_{1-2} \\ T_2 \\ T_{2-3} \\ T_3 \\ T_{s,in} \end{pmatrix} \quad (9)$$

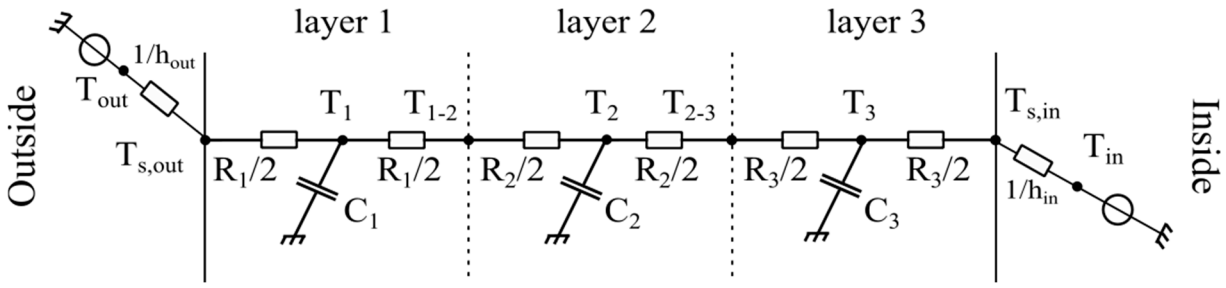

Figure 8. *RC model* structure for the *6R3C model*.

The system of Equations (9) has been solved using a backward Euler method. However, the *6R3C model* is not sufficiently accurate. The number of nodes in each layer is chosen to make the *RC model* sufficiently accurate. The first and third layers (plywood) are divided into five nodes, and the second layer (PUR) is divided into eleven nodes. The model is called the *24R21C model*.

3.5. Model Validation

The model was validated for cases encountered in experimental tests. These were divided into two categories: *cloudy days* and *sunny days*, as shown in Figure 4. The condition to validate the model is its ability to accurately reproduce the thermal behaviour of the wall on both typical days. To do this, the results obtained by simulating the *24R21C model* were compared with those obtained using the *reference model* for two types of boundary conditions.

The comparison of the model results was based on the study of the mean absolute deviations (MAD), i.e., the mean of the absolute value of the difference between the *reference model* and the *24R21C model*. The MAD for the *cloudy day* and for the *sunny day* are presented in Figure 9. This comparison was made for boundary conditions *BC1*. The results are similar for boundary conditions *BC2* (sensors S_2, $S_{2\text{-}3}$ and S_{in} only).

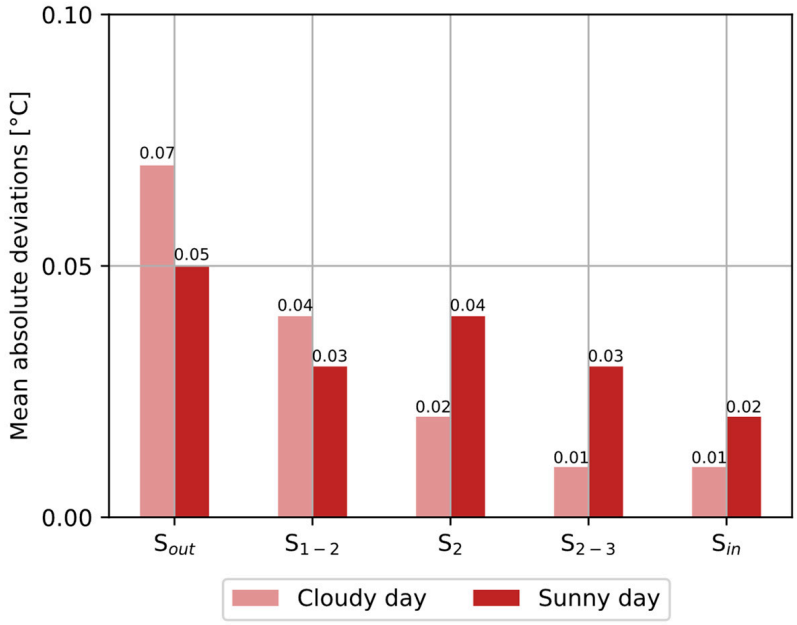

Figure 9. Validation of the *24R21C model*.

The *24R21C model* has a good accuracy for all sensors and both weather conditions. The largest error is for S_{out}.

4. Identification Technique

4.1. Principle of the Inverse Method

The principle of the inverse method is illustrated in Figure 10. On the one hand, experimental reference data (synthetic or measured) were available (T^{sensor}), and on the other hand, temperatures calculated by the *24R21C model* defined above (T^{model}) were generated.

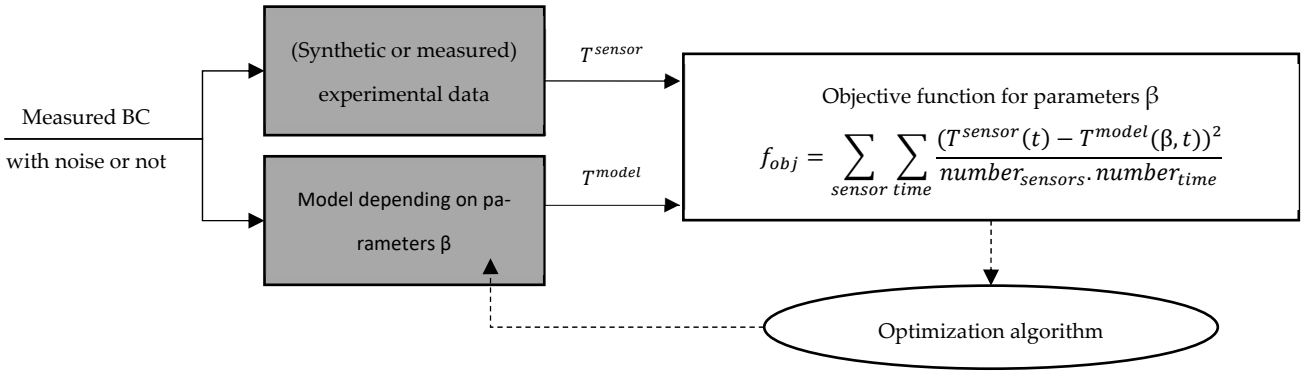

Figure 10. Principle of inverse method, adapted from [54].

The aim was to find the values of the physical parameters β defined in the *24R21C model*, so that the calculated temperatures fitted as close as possible to the experimental values. To achieve this, the inverse method consisted of minimizing the objective function defined in Figure 10. This function was minimized using the Nelder–Mead algorithm [55]. Different initial values were tested to avoid local minima.

The aim was to estimate the physical parameters (λ and $\rho.c$) of each layer and then calculate the *R*- and *C*-values of the walls using Equation (1).

4.2. Calculation of Uncertainties

Two sources of uncertainty were assessed: the uncertainty of the inverse method and model and the uncertainty linked to the boundary conditions. To assess the uncertainty due to the inverse method and model, an identification was performed using the "synthetic data without noise" (synthetized with the measured boundary conditions, as shown in Figure 3). As the theoretical values of R and C are known, the difference between the estimated values and the theoretical values provided the uncertainty of the inverse method.

In order to assess the uncertainty due to the boundary conditions, the identification was carried out with the "synthetic data with noise"; i.e., it included the measurement uncertainties. A white noise was applied to all the boundary conditions (T_{out}, T_{in}, T_b, Q_{SW}) and to the heat transfer coefficients ($h_{conv,out}$, h_{in}), given the associated uncertainties mentioned above. ε_{SW} and ε_{LW} were randomly generated, considering their respective uncertainties. More than 50 tests were performed with a randomly selected noise, with boundary conditions *BC1* and *BC2*.

The total uncertainty is equal to the uncertainty of the inverse method and model plus the uncertainty due to the boundary condition measurements. The uncertainty of the inverse method and model is the difference between the theoretical values and the estimated values in the case of the data "without noise". The uncertainty due to boundary condition measurements is defined as two times the standard deviation of the data "with noise", so that 95% of the estimates was included.

5. Results

First, the inverse method described in Section 4.1 was applied to synthetic data with boundary conditions *BC1* (see location in Figure 6). The effect of measurement uncertainty was investigated. Then, the method was applied to synthetic data considering boundary conditions *BC2* (see location in Figure 6). Finally, the method was applied to measured experimental data.

5.1. Application to Synthetic Data

5.1.1. Influence of the Heat Transfer Coefficients and Absorptivity

As shown in [31,46], heat transfer coefficients vary depending on the chosen correlation. The accuracy of the coefficients is also affected by the measurement uncertainty. It is therefore important to ensure that the uncertainty in the transfer coefficients does not have too large an effect on the output of the models, i.e., the calculated temperatures.

Given the uncertainties defined in Sections 2 and 3, it is possible to calculate the influence of the variation of each heat transfer coefficient during the typical *sunny day* and the typical *cloudy day* on the outputs of the *RC model*, as shown in Figure 11. In this case, results are obtained with boundary conditions. This influence is measured by calculating the difference between the temperatures calculated by the model when the parameter is equal to its upper limit and to its lower limit. The result for the *24R21C model* is shown in Figure 11.

Figure 11 shows that S_{out} and $S_{1\text{-}2}$ are very sensitive to α_{SW} and $h_{conv,out}$ variations during *sunny* and *cloudy days*. The results from sensors S_{out} and $S_{1\text{-}2}$ were rejected because α_{SW} and $h_{conv,out}$ were not known with high accuracy. Uncertainty may have had a negative impact on the identification. S_2 also appears to be sensitive on sunny days.

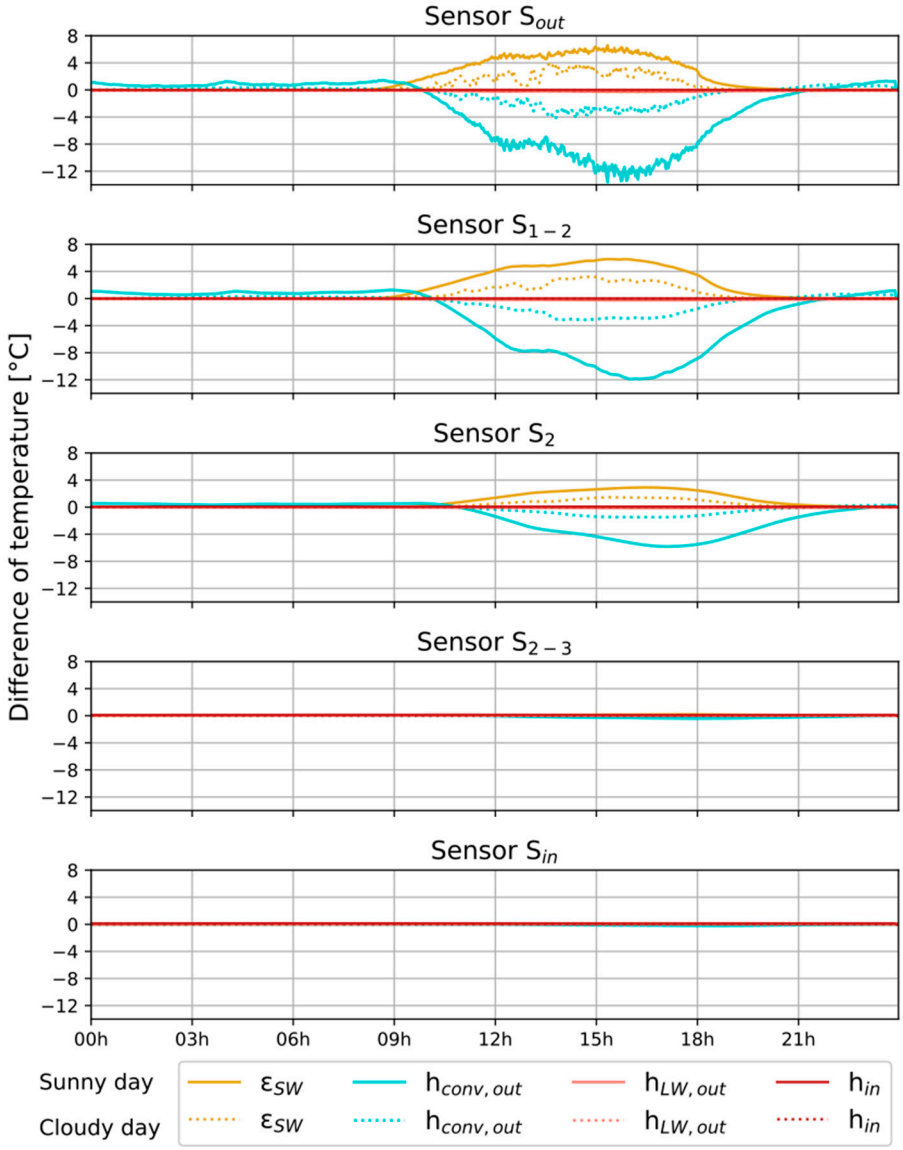

Figure 11. Study of the impact of the variation of heat transfer coefficients during the *cloudy day* and the *sunny day*.

5.1.2. Sensitivity According to Parameters to Be Identified

With boundary conditions *BC1*, a sensitivity analysis was carried out to investigate the variation in the response of the sensors to variations in the unknown physical parameters λ and $\rho.c$. This analysis provides information on the feasibility of estimating all the parameters simultaneously. The reduced sensitivities S^* were calculated according to Equation (10) [56]:

$$S_i^*(t,\beta) = \beta_i \frac{\partial T_k}{\partial \beta_i}(t,\beta) = \overline{\beta_i} \frac{T_k(t,\beta,\ \beta_i^+) - T_k(t,\beta,\ \beta_i^-)}{\beta_i^+ - \beta_i^-} \quad (10)$$

where β_i is the parameter of interest and $\overline{\beta_i}$, β_i^+ and β_i^- are the mean value, upper and lower limits (±10 %), respectively.

The variations of λ_{pl}, λ_{PUR}, $(\rho.c)_{pl}$ and $(\rho.c)_{PUR}$ were evaluated. The reduced sensitivities versus time are plotted in Figure 12. for the *24R21C model* during the *cloudy* and the *sunny days* described in Figure 4.

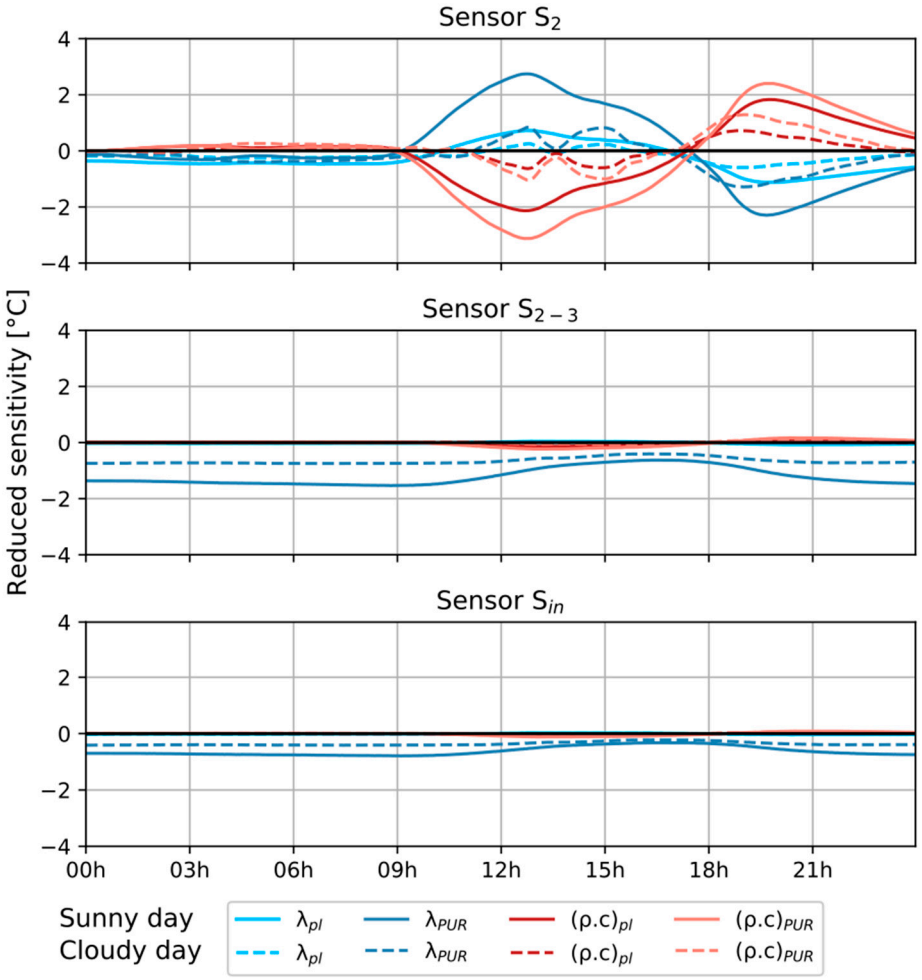

Figure 12. Sensitivity analysis of the parameters estimated during both typical days (*BC1*).

It seems clear that the reduced sensitivities of the four thermal properties are high for sensor S_2. The temperature measured at the location of sensor $S_{2\text{-}3}$ is only sensitive to the parameter λ_{PUR}. Sunny days seem to be the most convenient for the identification of the parameters, since the wall is more thermally stressed due to the solar radiation. The identification dataset should therefore contain sunny days to identify both *R*- and *C*-values.

The sensor S_{in} cannot be considered as a relevant sensor location, since the sensitivity to the parameters is rather low. Moreover, the measurement of surface temperatures is challenging and has a higher experimental uncertainty than the temperature inside walls. The temperature difference between the wall surface and the air is so small that in most cases it is close to the measurement uncertainty (±0.15 °C). Therefore, only sensors S_2 and $S_{2\text{-}3}$ are selected for identification. Figure 12 shows that some parameters may be correlated. This assumption is confirmed by looking at the correlation matrix of the two sensors (using a column-vector of sensitivities [54]) and during the *ROLBS case* shown in Table 3. All parameters cannot be estimated simultaneously, as $(\rho.c)_{pl}$ and $(\rho.c)_{PUR}$ are strongly correlated.

Table 3. Correlation matrix.

	λ_{pl}	λ_{PUR}	$(\rho.c)_{pl}$	$(\rho.c)_{PUR}$
λ_{pl}	1	−0.24	0.24	−0.03
λ_{PUR}		1	−0.05	0.16
$(\rho.c)_{pl}$			1	−0.95
$(\rho.c)_{PUR}$				1

However, according to theoretical calculations, 96% of the resistance is due to the insulation level of the polyurethane layer (λ_{PUR}) and 90% of the capacity is due to the capacity of the plywood layers $(\rho.c)_{pl}$. The identification will therefore focus on λ_{PUR} and $(\rho.c)_{pl}$. While λ_{pl} and $(\rho.c)_{PUR}$ are assumed to be equal to the theoretical value defined in Table 1, as an error in these values would have a limited effect on the estimated *R*- and *C*-values.

5.1.3. Identification Results with Synthetic Data and Boundary Conditions *BC1*

In this part, the T^{sensor} values in Figure 10 are synthetic data generated by the *reference model*. Boundary conditions during this test are boundary conditions *BC1* (see Section 2.3). Identification was applied to sensors S_2 and $S_{2\text{-}3}$. As shown in the previous section, S_{out} and $S_{1\text{-}2}$ were not used for identification due to the high influence of ill-defined model parameters, and S_{in} was rejected due to its low sensitivity. The *R*- and *C*-values were calculated simultaneously by estimating λ_{PUR} and $(\rho.c)_{pl}$.

The accuracy of the identification technique applied to the *24R21C model* was assessed by comparing the differences between the identified values and *R* and *C* (see Section 2.1). Figure 13 shows the result of the identification of the thermal characteristics of the wall with and without noise according to the *24R21C model*. The results are given as the difference between the estimated value and the theoretical target value. The graph has box plots to be read statistically. The crosses represent the mean value. The box extends from the first to the third quartile. The line in the middle indicates the median. The whiskers are a function of the inter-quartile range and the extreme values. Each black dot represents an estimate.

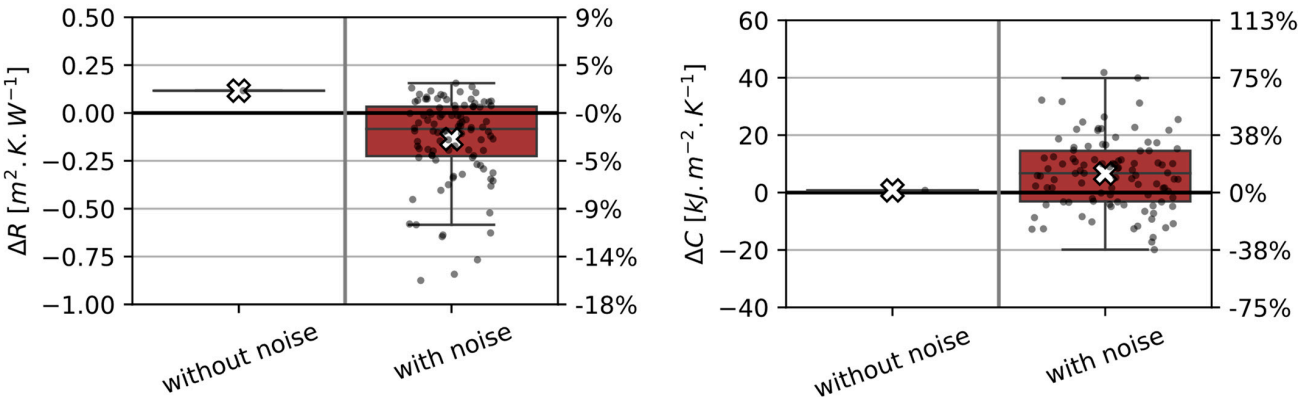

Figure 13. Estimation of *R*- and *C*-values—data with and without noise—*BC1*.

In terms of identification applied to synthetic data without noise, the *C*- and *R*-values are accurately estimated. The difference in estimation of the *C*-value is +0.75 kJ.m^{-2}.K^{-1} (+1%) compared to the theoretical value. The *R*-value is estimated to be +0.12 m^2.K.W^{-1} (+2%) higher than the theoretical value.

When noise is applied, the results are scattered. Half of the estimated resistances are between −4% and +1% of the theoretical value, but more extreme values occur. The error can reach up to −0.9 m^2.K.W^{-1} or −16%. Regarding capacities, the results are also scattered. Half of the estimated capacities are between −5% and +27% of the theoretical value. The error can reach up to 79%.

The total uncertainty can be calculated as shown in Section 4.2. The uncertainties are ±0.6 m^2.K.W^{-1} (10% error) for the *R*-value and ±26 kJ.m^{-2}.K^{-1} (48% error) for the *C*-value.

This indicates that identification from the measurement of the outer boundary conditions is not possible, because the uncertainties in the measurement of the boundary conditions and the heat transfer coefficients are too large in this case study. In the following section, a method is proposed to overcome these uncertainties.

5.1.4. Application to Synthetic Data with Boundary Conditions *BC2*

A similar methodology to that presented in Section 5.1.3 was used to assess the robustness of the identification with boundary conditions *BC2* (shown in Figure 6). As the outer boundary conditions is placed at the interface between the plywood and the polyurethane, the sensor S_2 is no longer sensitive to the thermal capacity of the plywood (Figure 14). However, sensor $S_{2\text{-}3}$ is sensitive enough to the thermal capacity when active heating is applied with a relatively rapid change in the indoor temperature (see the dashed line in Figure 14). This sensitivity is small but greater than the uncertainty of temperature sensors (over 0.15 °C). The limited influence of the indoor heat transfer coefficient was also observed (as in Figure 11). Therefore, the identification procedure was applied to sensors S_2 and $S_{2\text{-}3}$. The *R*- and *C*-values were calculated simultaneously by estimating λ_{PUR} and $(\rho.c)_{pl}$.

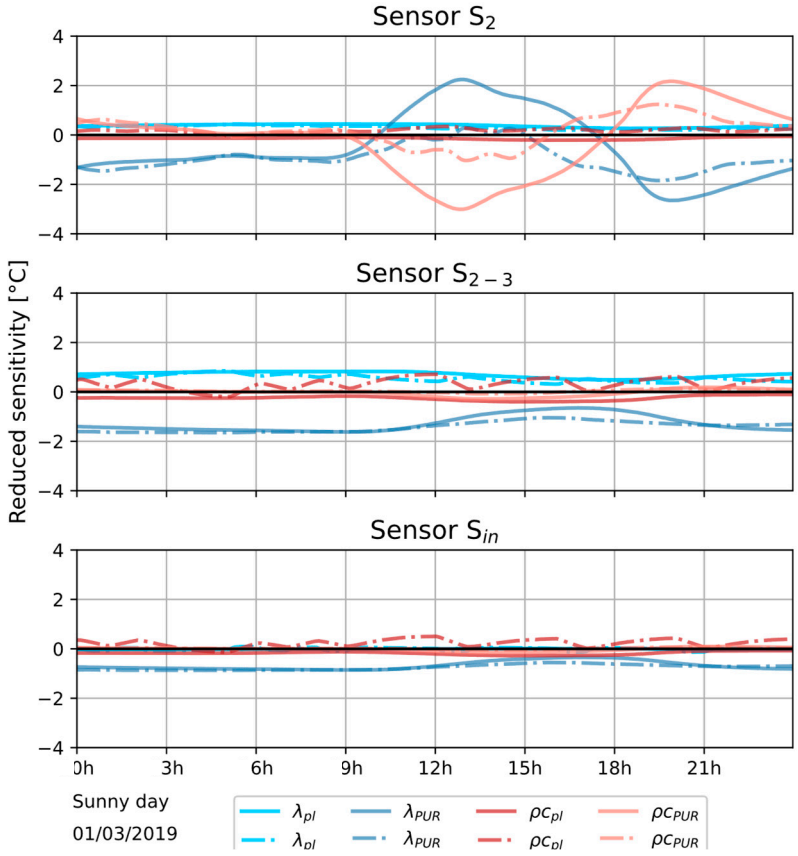

Figure 14. Sensitivity analysis of the parameters to be estimated with free floating conditions (*sunny day*) and with active heating (1 March 2019) with *BC2*.

The accuracy of the identification technique was assessed by comparing the differences between the estimated values of *R* and *C* (see Section 2.1). Figure 15 shows the result of the identification of the thermal characteristics of the wall with and without noise using boundary conditions *BC2*.

When the identification is applied to synthetic data without noise, the *R*-value is slightly underestimated by 2% and the *C*-value is also slightly underestimated by 1%. When noise is applied, the difference between the identified resistance and the theoretical value is about -0.15 m^2.K.W^{-1} or -2.5% for all estimates. For the capacities, the difference is also rather small (always less than 1 kJ.m^{-2}.K^{-1} or 1% error).

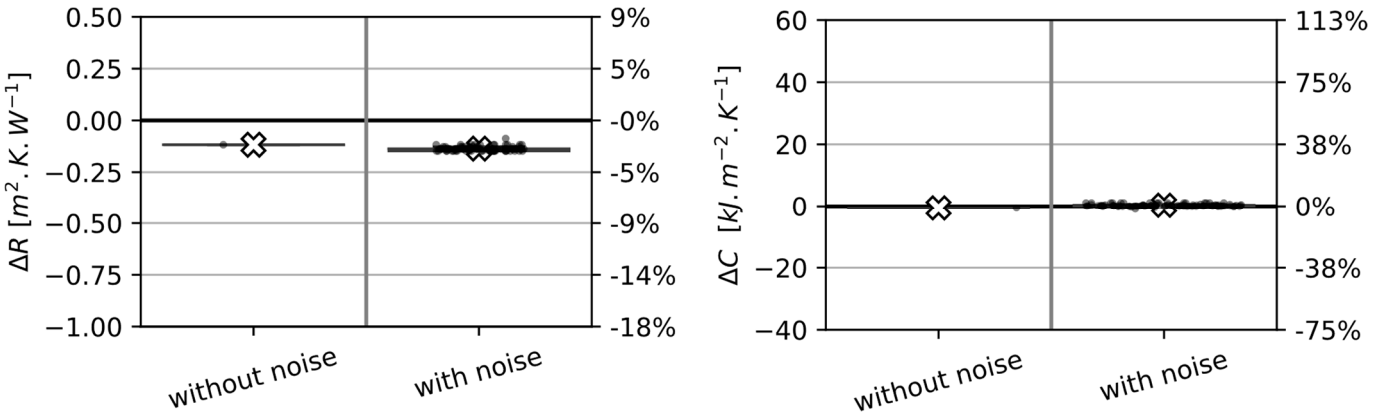

Figure 15. Estimation of *R*- and *C*-values—data with and without noise—*BC2*.

The total uncertainty can be calculated as shown in Section 4.2. The uncertainties for *24R21C model* are ±0.15 m^2.K.W^{-1} (3% error) for *R*-values and ±1.5 kJ.m^{-2}.K^{-1} (3% error) for *C*-values. The use of boundary conditions *BC2* greatly improves the accuracy of the *R*- and *C*-value estimation.

5.2. Application to Measured Experimental Data

In order to validate the previous observations, the identification methods were tested on measured experimental data. The wall properties were estimated from the measured experimental data. The identification results are shown in Figure 16. The grey area represents the range of theoretical values with the uncertainties defined in Section 2.1. The light pink rectangle represents the range of estimated *R*- and *C*-values, with the boundary condition *BC1*, and the deep pink rectangle represents the range of estimated *R*- and *C*-values, with the boundary condition *BC2*.

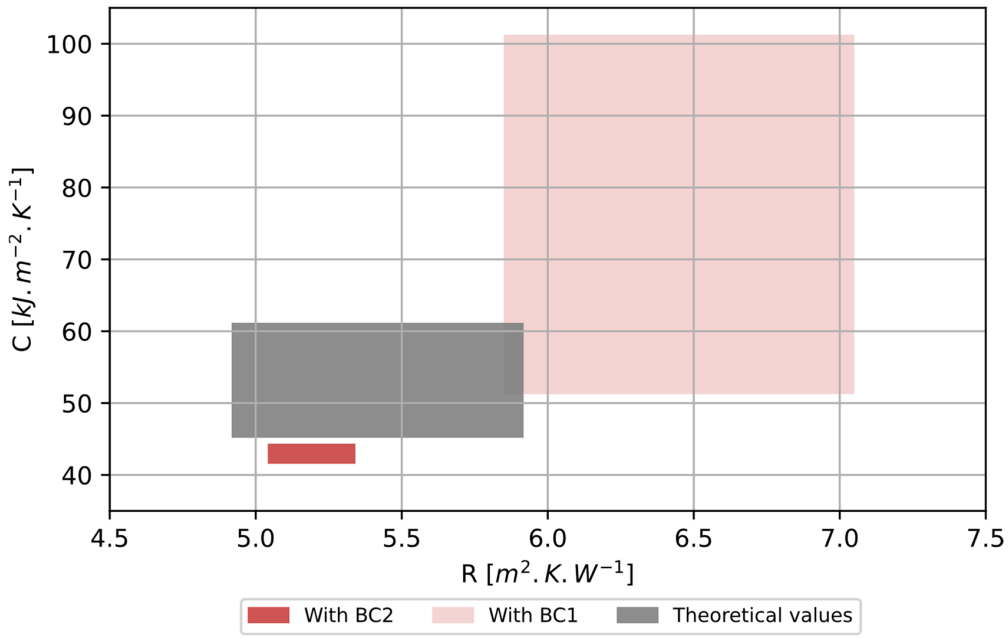

Figure 16. Estimation of *R*- and *C*-values from measured experimental data and using outside and inside boundary conditions.

It can be seen that the results with *BC1* encompass extended ranges, as the uncertainties are large in this case. Moreover, the *R*-value is significantly overestimated.

The area corresponding to boundary conditions *BC2* is smaller and closer to the theoretical area. The resistance can be estimated between 5.05 and 5.35 $m^2.K.W^{-1}$. The estimated capacities are slightly lower than the theoretical capacity, between 41.5 and 44.5 $kJ.m^{-2}.K^{-1}$. The difference between theory and estimate may be due to the uncertainty of the model, the duration of the wall loading, the reduced sensitivity to the plywood thermal capacity or the theoretical values estimated from tabulated data.

To verify that the *RC model* correctly reproduces the thermal behaviour of the wall, the validation part of the *ROLBS case* was used (see data in Figure 3). Figure 17 shows the temperatures measured by sensors S_2 and $S_{2\text{-}3}$ and the temperature estimated by the model and their residuals. The residuals are small, indicating that the model correctly reproduces the thermal behaviour of the wall.

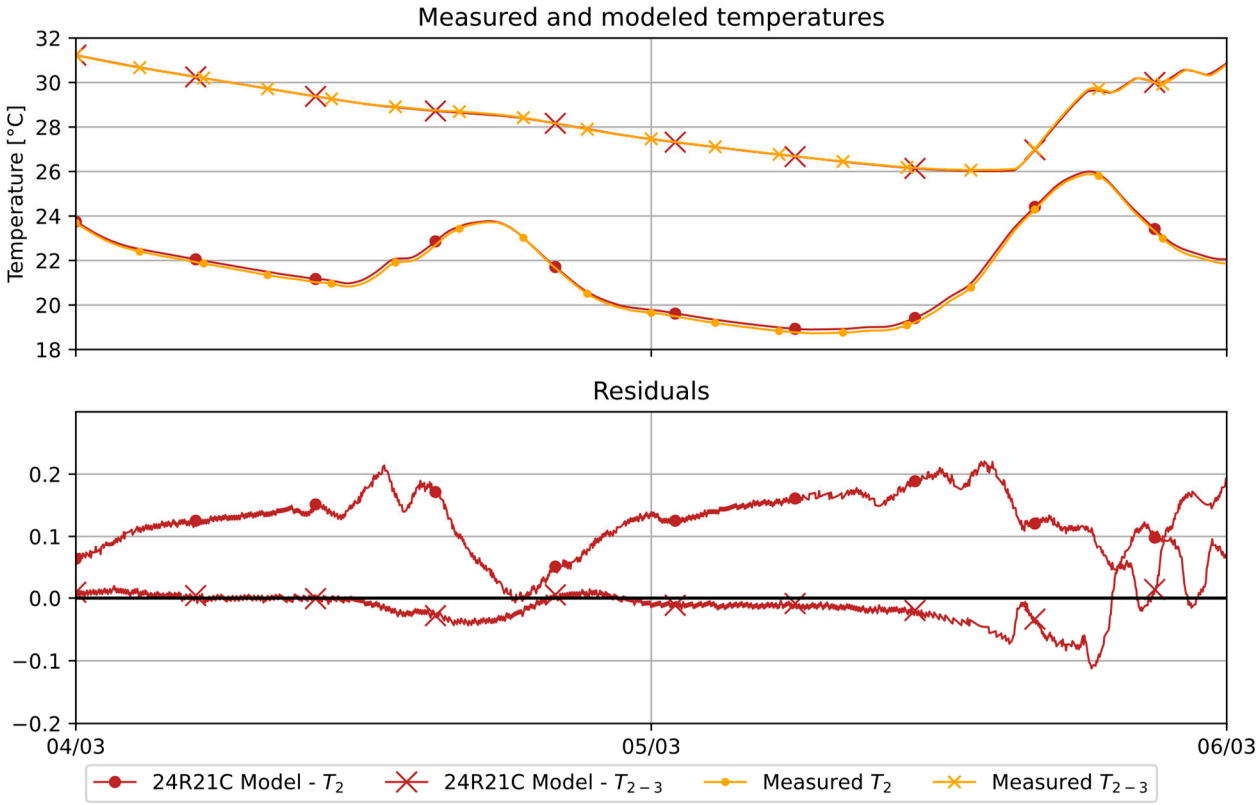

Figure 17. Temperature measured in the wall and estimated by the model and the residuals.

6. Discussions

Table 4 summarizes the results. The main differences between the identification results lie in the choice of boundary conditions. It is shown that when boundary conditions *BC1* are chosen, the uncertainties are so large that the results are unusable. When boundary conditions *BC2* are considered, the *RC model* estimates the resistance and capacity with acceptable uncertainties.

A procedure is provided as shown in Figure 18. Two cases are highlighted regarding the boundary conditions *BC1* or *BC2*. If *BC2* is chosen, special attention must be paid to the location of the sensors in order to minimize their sensitivity to the boundary conditions, while setting the experimental design. Once the sensors have been installed and their uncertainty calculated, the parameters to be estimated can be derived from a second sensitivity study. The uncertainty of identification associated with these boundary conditions can then be calculated. If the accuracy is satisfactory, the experiment is performed with dynamic boundary conditions.

Table 4. Results of estimation.

	Parameter		***RC***	**COMSOL**
Modelling	Space	Number	21 nodes	28 elements
	Time	Boundary conditions	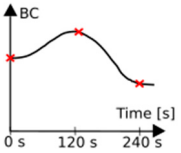	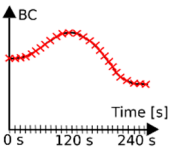
		Time step	120 s	10 s
Identification results	*BC1* 	*R*	±10%	
		C	±47%	
	BC2 	*R*	±3%	
		C	±3%	

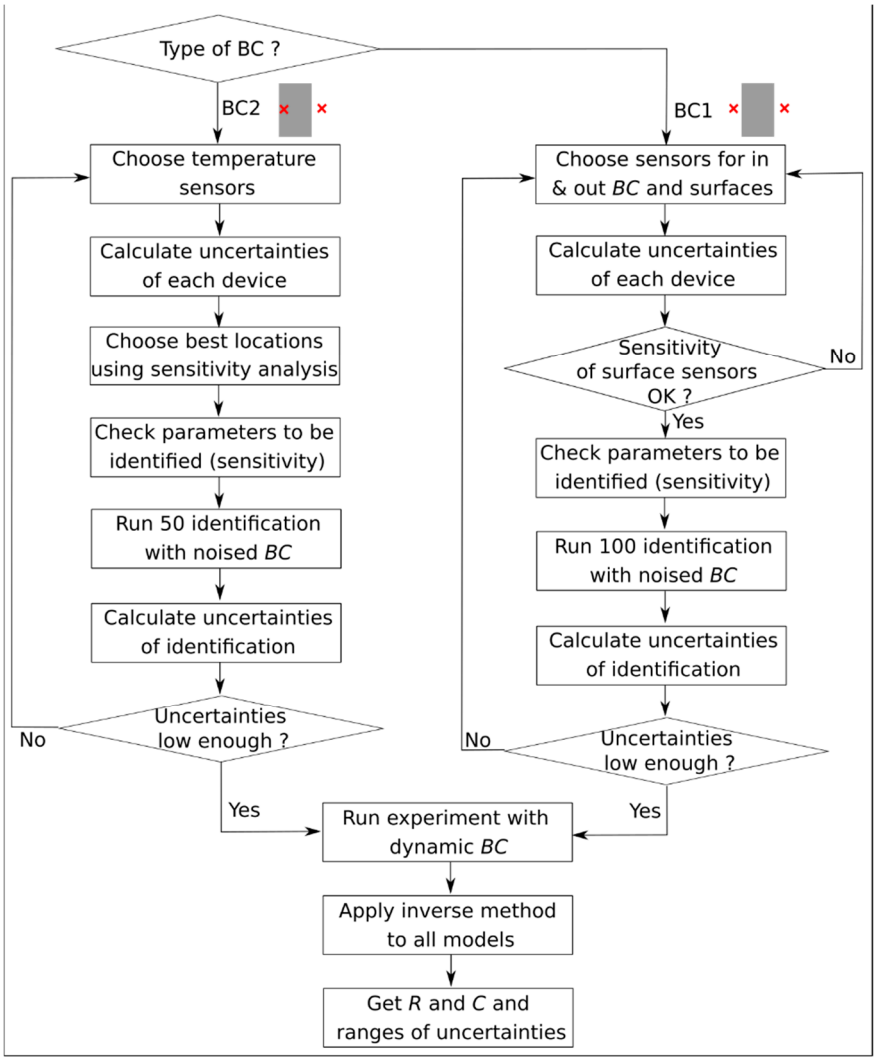

Figure 18. Procedure for experimental design.

If *BC1* is chosen, attention must be paid to the accuracy of the sensors measuring the boundary conditions, as this has been shown in this article to be a limitation of this method. The calculation of the uncertainties of the parameter estimation allows the method to be validated or not.

7. Conclusions

The objective of this article has been to evaluate the one-dimensional heat transfer in a multilayer wall under real weather conditions using temperature sensors.

A sensitivity analysis was performed to reject the sensors that were too sensitive to parameters defined with low accuracy, such as the internal and external radiative and convective heat transfer coefficients and the external solar absorptivity. Differences up to 8 °C could be observed, depending on the assumptions. This step determined that two of the five sensors were useful.

To increase the confidence in estimated parameters, the identification was limited to the parameters contributing the most to the global thermal properties of the wall assembly. Therefore, it was found that estimating the thermal conductivity of the insulation layer and the specific heat capacity of the wooden layer was enough for assessing accurately the *R*- and *C*-values of the wall.

The parameter estimation method was carried out with two types of boundary conditions: either the outside boundary conditions (air temperature, brightness temperature and solar radiation) or the temperature measured a few centimeters below the outer surface of the wall (intrusive sensor). The uncertainty on the estimated parameters obtained with the outside boundary conditions was very large (over 1 $m^2.K.W^{-1}$ for *R*) compared to the one obtained by using an intrusive sensor (0.3 $m^2.K.W^{-1}$). Using an intrusive sensor, with adapted sensitivity to the applied thermal loads, considerably reduced the uncertainty of the estimation. Considering the results, the estimated resistance fell within the range of variation defined from the theoretical values. The estimated capacity was slightly lower than the theoretical value.

Finally, this article provided guidelines for measuring thermal properties of homogenous, highly insulated multilayer walls with uncertainties. It requires a rough knowledge of the wall structure. A procedure is presented in Figure 18. It helps to confirm the relevance of carrying out experimental tests according to the location of sensors and the expected uncertainty of the measurements. This methodology could also be applied to highly insulated heavyweight walls to see if the same conclusions can be drawn about the ability of the model to estimate thermal characteristics.

Author Contributions: Conceptualization, M.R., J.L.D., P.S. and M.D.; methodology, M.R., J.L.D., P.S. and M.D.; software, M.R.; validation, M.R., J.L.D., P.S. and M.D.; formal analysis, M.R.; data curation, M.R.; writing—original draft preparation, M.R.; writing—review and editing, M.R., J.L.D., P.S. and M.D.; supervision, J.L.D. and P.S.; project administration, funding acquisition, P.S. All authors have read and agreed to the published version of the manuscript.

Funding: This research was funded by the European Union and the French region Nouvelle-Aquitaine with the industrial partners TIPEE Platform and EDF (Research Project "CITEE—Innovative components for building envelopes"). The authors are grateful for their technical and financial support.

Data Availability Statement: The code and data can be found at: https://gitlab.univ-lr.fr/jledreau/Inverse_Wall1D (accessed on 14 November 2024).

Acknowledgments: A special thanks goes to Michel Burlot, David Gaillard and Laurent Servant for their involvement in the experimental work and to Denis Maillet and Mathilde Colmet-Daage for their relevant advice.

Conflicts of Interest: There are no conflicts of interest.

Nomenclature

c	Specific heat capacity, $J.kg^{-1}.K^{-1}$	Q	Heat flux density, $W.m^{-2}$
C	Total thermal mass, $J.m^{-2}.K^{-1}$	R	Thermal resistance, $m^2.K.W^{-1}$
d	Wind direction, °	S	Sensor
e	Thickness of a layer, m	t	Time, s
h	Heat transfer coefficient, $W.m^{-2}.K^{-1}$	T	Temperature, °C or K
L	Thickness of wall, m	v	Velocity, $m.s^{-1}$

MAD	Mean absolute deviation, °C	x	Space variable, m
Greek symbols			
α	Absorptivity, -	λ	Thermal conductivity, $W.m^{-1}.K^{-1}$
β	List of parameters to be estimated	ρ	Density, $kg.m^{-3}$
ε	Emissivity, -	σ	Stefan-Boltzmann constant, $W.m^{-2}.K^{-4}$
Index and Exponent			
$\rightarrow \mid$	Received by device	PUR	Polyurethane
b	Brightness	pyrgeo	Pyrgeometer
conv	Convection	out	Outdoor
in	Indoor	S	Surface
LW	Longwave radiation	SW	Shortwave radiation
pl	Plywood		

References

1. Meiss, A.; Feijó-Muñoz, J. The energy impact of infiltration: A study on buildings located in north central Spain. *Energy Effic.* **2015**, *8*, 51–64. [CrossRef]
2. Eleftheriadis, G.; Hamdy, M. Impact of building envelope and mechanical component degradation on the whole building performance: A review paper. *Energy Procedia* **2017**, *132*, 321–326. [CrossRef]
3. Asan, H.; Sancaktar, Y. Effects of Wall's thermophysical properties on time lag and decrement factor. *Energy Build.* **1998**, *28*, 159–166. [CrossRef]
4. *NF EN 12939*; Thermal Performance of Building Materials and products—Determination of Thermal Resistance by Means of Guarded Hot Plate and Heat Flow Meter Methods—Thick Products of High and Medium Thermal Resistance. British Standards Institution: London, UK, 2000.
5. *NF EN 12667*; Thermal Performance of Building Materials and Products—Determination of Thermal Resistance by Means of Guarded Hot Plate and Heat Flow Meter Methods—Products of High and Medium Thermal Resistance. British Standards Institution: London, UK, 2001.
6. Bienvenido-Huertas, D.; Moyano, J.; Marín, D.; Fresco-Contreras, R. Review of in situ methods for assessing the thermal transmittance of walls. *Renew. Sustain. Energy Rev.* **2019**, *102*, 356–371. [CrossRef]
7. *ISO 9869-1*; Thermal Insulation—Building Elements—In-Situ Measurement of Thermal Resistance and Thermal Transmittance—Part 1: Heat Flow Meter Method. International Organization for Standardization: Geneva, Switzerland, 2014.
8. Peng, C.; Wu, Z. In situ measuring and evaluating the thermal resistance of building construction. *Energy Build.* **2008**, *40*, 2076–2082. [CrossRef]
9. Teni, M.; Krstić, H.; Kosiński, P. Review and comparison of current experimental approaches for in-situ measurements of building walls thermal transmittance. *Energy Build.* **2019**, *203*, 109417. [CrossRef]
10. Beck, J.V.; Blackwell, B.; Clair, C.R.S. *Inverse Heat Conduction: Ill-Posed Problems*; Wiley: Hoboken, NJ, USA, 1985.
11. Beck, J.V.; Arnold, K.J. *Parameter Estimation in Engineering and Science*; Wiley: Hoboken, NJ, USA, 1977.
12. Orlande, H.R.; Fudym, O.; Maillet, D.; Cotta, R.M. *Thermal Measurements and Inverse Techniques*; CRC Press: Boca Raton, FL, USA, 2011. [CrossRef]
13. Defer, D.; Shen, J.; Lassue, S.; Duthoit, B. Non-destructive testing of a building wall by studying natural thermal signals. *Energy Build.* **2002**, *34*, 63–69. [CrossRef]
14. Sassine, E. A practical method for in-situ thermal characterization of walls. *Case Stud. Therm. Eng.* **2016**, *8*, 84–93. [CrossRef]
15. Rasooli, A.; Itard, L.; Ferreira, C.I. A response factor-based method for the rapid in-situ determination of wall's thermal resistance in existing buildings. *Energy Build.* **2016**, *119*, 51–61. [CrossRef]
16. Rasooli, A.; Itard, L. In-situ rapid determination of walls' thermal conductivity, volumetric heat capacity, and thermal resistance, using response factors. *Appl. Energy* **2019**, *253*, 113539. [CrossRef]
17. Gutschker, O. Parameter identification with the software package LORD. *Build. Environ.* **2008**, *43*, 163–169. [CrossRef]
18. Baker, P.; van Dijk, H. PASLINK and dynamic outdoor testing of building components. *Build. Environ.* **2008**, *43*, 143–151. [CrossRef]
19. Loussouarn, T.; Maillet, D.; Remy, B.; Schick, V.; Dan, D. Indirect measurement of temperature inside a furnace, ARX model identification. *J. Phys. Conf. Ser.* **2018**, *1047*, 012006. [CrossRef]
20. Jiménez, M.; Heras, M. Application of multi-output ARX models for estimation of the U and g values of building components in outdoor testing. *Sol. Energy* **2005**, *79*, 302–310. [CrossRef]
21. Naveros, I.; Ghiaus, C.; Ruíz, D.; Castaño, S. Physical parameters identification of walls using ARX models obtained by deduction. *Energy Build.* **2015**, *108*, 317–329. [CrossRef]
22. Limam, K.; Bouache, T.; Ginestet, S.; Popescu, L.O. Numerical and experimental identification of simplified building walls using the reflective Newton method. *J. Build. Phys.* **2018**, *41*, 321–338. [CrossRef]
23. Naveros, I.; Bacher, P.; Ruiz, D.; Jiménez, M.; Madsen, H. Setting up and validating a complex model for a simple homogeneous wall. *Energy Build.* **2014**, *70*, 303–317. [CrossRef]

24. Berger, J.; Orlande, H.R.; Mendes, N.; Guernouti, S. Bayesian inference for estimating thermal properties of a historic building wall. *Build. Environ.* **2016**, *106*, 327–339. [CrossRef]
25. Biddulph, P.; Gori, V.; Elwell, C.A.; Scott, C.; Rye, C.; Lowe, R.; Oreszczyn, T. Inferring the thermal resistance and effective thermal mass of a wall using frequent temperature and heat flux measurements. *Energy Build.* **2014**, *78*, 10–16. [CrossRef]
26. Rouchier, S.; Woloszyn, M.; Kedowide, Y.; Béjat, T. Identification of the hygrothermal properties of a building envelope material by the covariance matrix adaptation evolution strategy. *J. Build. Perform. Simul.* **2015**, *9*, 101–114. [CrossRef]
27. Wang, S.; Xu, X. Parameter estimation of internal thermal mass of building dynamic models using genetic algorithm. *Energy Convers. Manag.* **2006**, *47*, 1927–1941. [CrossRef]
28. Chaffar, K.; Chauchois, A.; Defer, D.; Zalewski, L. Thermal characterization of homogeneous walls using inverse method. *Energy Build.* **2014**, *78*, 248–255. [CrossRef]
29. Dall'O', G.; Sarto, L.; Panza, A. Infrared Screening of Residential Buildings for Energy Audit Purposes: Results of a Field Test. *Energies* **2013**, *6*, 3859–3878. [CrossRef]
30. de Rubeis, T.; Evangelisti, L.; Guattari, C.; De Berardinis, P.; Asdrubali, F.; Ambrosini, D. On the Influence of Environmental Boundary Conditions on Surface Thermal Resistance of Walls: Experimental Evaluation through a Guarded Hot Box. *Case Stud. Therm. Eng.* **2022**, *34*, 101915. [CrossRef]
31. Evangelisti, L.; Guattari, C.; Gori, P.; Vollaro, R.d.L.; Asdrubali, F. Experimental Investigation of the Influence of Convective and Radiative Heat Transfers on Thermal Transmittance Measurements. *Int. Commun. Heat Mass Transf.* **2016**, *78*, 214–223. [CrossRef]
32. François, A.; Ibos, L.; Feuillet, V.; Meulemans, J. Novel in Situ Measurement Methods of the Total Heat Transfer Coefficient on Building Walls. *Energy Build.* **2020**, *219*, 110004. [CrossRef]
33. Derbal, R.; Defer, D.; Chauchois, A.; Antczak, E. A simple method for building materials thermophysical properties estimation. *Constr. Build. Mater.* **2014**, *63*, 197–205. [CrossRef]
34. Spitz, C.; Mora, L.; Wurtz, E.; Jay, A. Practical application of uncertainty analysis and sensitivity analysis on an experimental house. *Energy Build.* **2012**, *55*, 459–470. [CrossRef]
35. *EN ISO 6946*; Building Components and Building Elements—Thermal Resistance and Thermal Transmittance—Calculation Method. International Organization for Standardization: Geneva, Switzerland, 2017.
36. Macdonald, I.A. Quantifying the Effects of Uncertainty in Building Simulation. Ph.D. Thesis, University of Strathclyde, Glasgow, UK, 2002.
37. CSTB. Règles Th-bat—Fascicule Matériaux (French Building Regulation). France, 2017. Available online: https://rt-re-batiment.developpement-durable.gouv.fr/IMG/pdf/2-fascicule_materiaux.pdf (accessed on 14 November 2024).
38. Ross, R.J. *Wood Handbook: Wood as an Engineering Material*; U.S. Dept. of Agriculture, Forest Service, Forest Products Laboratory: Madison, WI, USA, 2010; Volume 190.
39. Cattarin, G.; Causone, F.; Kindinis, A.; Pagliano, L. Outdoor test cells for building envelope experimental characterization—A literature review. *Renew. Sustain. Energy Rev.* **2016**, *54*, 606–625. [CrossRef]
40. Spampinato, L.; Calvari, S.; Oppenheimer, C.; Boschi, E. Volcano surveillance using infrared cameras. *Earth-Sci. Rev.* **2011**, *106*, 63–91. [CrossRef]
41. Orme, M. *Applicable Models for Air Infiltration and Ventilation Calculations*; AIVC: Vancouver, BC, Canada, 1999.
42. Madsen, H.; Bacher, P.; Bauwens, G.; Deconinck, A.H.; Reynders, G.; Roels, S.; Himpe, E.; Lethé, G. Thermal Performance Characterization using Time Series Data. In *IEA EBC Annex 58 Guidelines*; International Energy Agency: Paris, France, 2015.
43. Maillet, D.; André, S.; Batsale, J.-C.; Degiovanni, A.; Moyne, C. *Thermal Quadrupoles: Solving the Heat Equation Through Integral Transforms*; Wiley: Hoboken, NJ, USA, 2000.
44. Brun, A. Amélioration du confort d'été dans des bâtiments à ossature par ventilation de l'enveloppe et stockage thermique. Ph.D. Thesis, Université de Grenoble, Saint-Martin-d'Hères, France, 2011.
45. Khalifa, A.; Marshall, R. Validation of heat transfer coefficients on interior building surfaces using a real-sized indoor test cell. *Int. J. Heat Mass Transf.* **1990**, *33*, 2219–2236. [CrossRef]
46. Peeters, L.; Beausoleil-Morrison, I.; Novoselac, A. Internal convective heat transfer modeling: Critical review and discussion of experimentally derived correlations. *Energy Build.* **2011**, *43*, 2227–2239. [CrossRef]
47. Awbi, H.; Hatton, A. Natural convection from heated room surfaces. *Energy Build.* **1999**, *30*, 233–244. [CrossRef]
48. Defraeye, T.; Blocken, B.; Carmeliet, J. Convective heat transfer coefficients for exterior building surfaces: Existing correlations and CFD modelling. *Energy Convers. Manag.* **2011**, *52*, 512–522. [CrossRef]
49. ASHRAE Task Group. *Procedure for Determining Heating and Cooling Loads for Computerizing Energy Calculations: Algorithms for Building Heat Transfer Subroutines*; American Society of Heating, Refrigerating and Air-Conditioning Engineers: Peachtree Corners, GA, USA, 1976.
50. Sharples, S. Full-scale measurements of convective energy losses from exterior building surfaces. *Build. Environ.* **1984**, *19*, 31–39. [CrossRef]
51. Liu, Y.; Harris, D. Full-scale measurements of convective coefficient on external surface of a low-rise building in sheltered conditions. *Build. Environ.* **2007**, *42*, 2718–2736. [CrossRef]
52. COMSOL. COMSOL Multiphysics 5.5 Reference Manual. 2019. Available online: https://doc.comsol.com/5.5/doc/com.comsol.help.comsol/COMSOL_ReferenceManual.pdf (accessed on 14 November 2024).

53. Tsilingiris, P. Parametric space distribution effects of wall heat capacity and thermal resistance on the dynamic thermal behavior of walls and structures. *Energy Build.* **2006**, *38*, 1200–1211. [CrossRef]
54. Petit, D.; Maillet, D. Techniques inverses et estimation de paramètres. Partie 1. *Tech. Ing. Phys. Stat. Mathématique* **2008**, *42619210*, 1–18.
55. Nelder, J.A.; Mead, R. A Simplex Method for Function Minimization. *Comput. J.* **1965**, *7*, 308–313. [CrossRef]
56. Remy, B.; Degiovanni, A. Parameters estimation and measurement of thermophysical properties of liquids. *Int. J. Heat Mass Transf.* **2005**, *48*, 4103–4120. [CrossRef]